Materials Horizons

ROYAL SOCIETY OF CHEMISTRY

COMMUNICATION

View Article Online
View Journal | View Issue

Cite this: *Mater. Horiz.*, 2024, **11**, 5304

Received 12th June 2024,
Accepted 31st July 2024

DOI: 10.1039/d4mh00747f

rsc.li/materials-horizons

Key factors behind the superior performance of polymer-based NFA blends†

Elifnaz Sağlamkaya,[a] Mohammad Saeed Shadabroo,[a] Nurlan Tokmoldin,[ab] Tanner M. Melody,[c] Bowen Sun,[a] Obaid Alqahtani,[cd] Acacia Patterson,[c] Brian A. Collins,[c] Dieter Neher[a] and Safa Shoaee[*ab]

All-small molecule (ASMs) solar cells have great potential to actualize the commercialization of organic photovoltaics owing to their higher solubility, lesser batch-to-batch variety and simpler synthesis routes compared to the blend systems that utilize conjugated polymers. However, the efficiencies of the ASMs are slightly lacking behind the polymer: small molecule bulk-heterojunctions. To address this discrepancy, we compare an ASM blend ZR1:Y6 with a polymer:small molecule blend PM7:Y6, sharing the same non-fullerene acceptor (NFA). Our analyses reveal similar energetic offset between the exciton singlet state and charge transfer state (ΔE_{S_1-CT}) in ZR1:Y6 and PM7:Y6. In comparison to the latter, surprisingly, the ZR1:Y6 has noticeably a stronger field-dependency of charge generation. Low charge carrier mobilities of ZR1:Y6 measured, using space charge limited current measurements, entail a viable explanation for suppressed charge dissociation. Less crystalline and more intermixed domains as observed in the ZR1:Y6 system compared to polymer:Y6 blends, makes it difficult for NFA to form a continuous pathway for electron transport, which reduces the charge carrier mobility.

New concepts

This study investigates factors influencing free charge generation, decoupling the effect of the energetic landscape from morphology. We compare an all-small-molecule system, ZR1:Y6, with polymer-small-molecule systems PM7:Y6 and PM6:Y6. PM7:Y6 and ZR1:Y6 show similar energetic offsets, whereas PM6:Y6 has a higher offset compared to the other two. Despite the similar offsets, the field dependency of charge generation differs in ZR1:Y6. Remarkably, across all three systems, the activation energy for charge generation remains consistent, yet the dissociation rate coefficient is notably lower in the ZR1:Y6 blend. Our findings highlight the crucial role of structural order and π–π stacking in polymer blends, enhancing charge carrier mobility and reducing recombination losses. This morphological influence is starkly evident in the ZR1:Y6 blend, where, despite having lower energetic disorder, the system is still characterized by lower mobility and higher field dependency of charge generation due to less crystalline and more intermixed domains. Our work suggests that morphological engineering can adjust the minimum required donor/acceptor energetic offset for efficient charge generation.

Introduction

Batch-to batch consistency and easy processing conditions are imperative for commercialization of organic solar cells.[1] The best efficiencies in the laboratories are so far achieved with the polymer donor and small molecule non-fullerene acceptors (NFA). However, synthesis and purification of the polymers are costly processes, and the polydispersity indexes[2] and molecular masses[3] vary between batches and providers. Small molecules have inherent advantages in the mass production thanks to their high solubility, less batch-to-batch variability and less complex synthesis routes.[4] Scalability of the organic devices requires finding alternative fabrication methods to spin-coating, such as evaporation. All-small molecule (ASM) blends can be fabricated by evaporation,[5,6] unlike the polymer blends. Furthermore, energetic disorder inherent in the polymers presents a notable obstacle in developmental endeavors, posing a critical research challenge. Disorder induced Gaussian tails of the density of states (DOS) extend deep in to the energy gap and reduce the charge transfer state energy (E_{CT}), causing radiative open-circuit voltage (V_{OC}) losses ($\Delta V_{OC_{rad}}$).[7] Furthermore, energetic disorder also increases the non-radiative recombination (rate constant), as predicted by the Marcus–Levich–Jortner theory,[8] which reflects in the V_{OC} losses ($\Delta V_{OC_{nrad}}$) and the fill factor (FF). Thus lower energetic disorder values are expected to decrease both types of V_{OC} losses and improve FF.[9,10] Despite of these advantages, the efficiencies of the ASMs are still somewhat lacking behind the polymer: small molecule single junctions (17–16% *vs.* 19–18%).[11–14]

[a] *Institute of Physics and Astronomy, University of Potsdam, Karl-Liebknecht-Str. 24-25, 14476 Potsdam-Golm, Germany. E-mail: shoai@uni-potsdam.de*
[b] *Paul-Drude-Institut für Festkörperelektronik Leibniz-Institut im Forschungsverbund Berlin e.V., Hausvogteiplatz 5-7, 10117 Berlin, Germany*
[c] *Department of Physics and Astronomy, Washington State University, 100 Dairy Road, Pullman, WA, 99164, USA*
[d] *Department of Physics, Prince Sattam bin Abdulaziz University, Alkharj, 11942, Kingdom of Saudi Arabia*

† Electronic supplementary information (ESI) available. See DOI: https://doi.org/10.1039/d4mh00747f

2,2′-((2*Z*,2′*Z*)-((12,13-bis(2-ethylhexyl)-3,9-diundecyl-12,13-dihydro-[1,2,5]thiadiazolo[3,4 e]thieno[2″,3″:4′,5′]thieno[2′,3′:4,5]pyrrolo[3,2-g]thieno[2′,3′:4,5]thieno[3,2-*b*]indole-2,10-diyl)bis(methanylylidene))bis(5,6-difluoro-3-oxo-2,3-dihydro-1*H*-indene-2,1-diylidene))dimalononitrile (Y6) is a ADA′DA (A = acceptor unit, D = donor unit) type NFA molecule that has a curved geometric conformation. The shape of the molecule enables a 3D network morphology in films where the D and A units of neighboring Y6 molecules stack on top of each other. Consequently, charge transport in Y6 is ambipolar and efficient. In addition, Y6 excitons are delocalized over more than one molecule which reduces the exciton binding energy (E_b).[15–17] Owing to a smaller than typical E_b in Y6, bulk charge photogeneration, whilst not too efficient is observed in the single component Y6 devices.[18,19] On the other hand, bulk heterojunction (BHJ) blends of Y6 with poly[(2,6-(4,8-bis(5-(2-ethylhexyl-3-fluoro)thiophen-2-yl)-benzo[1,2-*b*:4,5-*b*′]dithiophene))-*alt*-(5,5-(1′,3′-di-2-thienyl-5′,7′-bis(2-ethylhexyl)benzo[1′,2′-*c*:4′,5′-*c*′]dithiophene-4,8-dione)] (PM6) achieved near unity charge generation yields and field and temperature independent charge dissociation, despite of the small D/A energy offset.[20–22] Morphological studies on the most efficient polymer:Y6 blends revealed the polymers do not disturb the 3D networks in Y6 domains and both the donor and the Y6 aggregates adapt a face-on alignment to the substrate.[23–25] Spatial confinement of the opposite charges in the donor and Y6 prevents the fast recombination of the free charges.[19] Moreover, polymer chains of the donor materials provide conductive channels between different Y6 domains, enabling high charge carrier mobilities.[26] Favorable morphologies in the polymer:Y6 blends enable fast charge dissociation rates, concomitantly suppressing free charge recombination.[27] Obtaining equally optimal morphologies with efficient percolation pathways in ASM blends is more challenging. ASM blends can suffer from large crystalline domains due to over aggregation of one or both of the components.[1,12,28]

Herein we show a systematic comparison between an ASM blend based on 5,5′-[[4,8-bis[5-(2-butyloctyl)-2-thienyl]dithieno-[2,3-*d*:2′,3′-*d*′]benzo[1,2-*b*:4,5-*b*′]dithiophene-2,6-diyl]bis([3′-octyl-[2,2′-bithiophene]-5″,5-diyl)methylidyne]]bis[3-hexyl-2-thioxo-4-thiazolidinone] (ZR1) with polymer-small molecule blends based on: poly[(2,6-(4,8-bis(5-(2-ethylhexyl-3-chloro)thiophen-2-yl)-benzo-[1,2-*b*:4,5-*b*′]dithiophene))-*alt*-(5,5-(1′,3′-di-2-thienyl)-5′,7′-bis(2-ethylhexyl)benzo[1′,2′-*c*:4′,5′-*c*′]dithiophene-4,8-dione)] (PM7) and PM6, all using the same Y6 NFA. As expected, ZR1:Y6 exhibits low energetic disorder compared to the polymer:Y6 blends. Despite the low disorder, low electron mobility is measured for ZR1:Y6. From temperature dependent electroluminescence (T-EL) measurements, the ΔE_{S_1-CT} energy offset is estimated to be similar for both PM7:Y6 and ZR1:Y6 blends, which sits moderately smaller than the PM6:Y6 offset. The largest free charge recombination coefficient is measured for ZR1:Y6, followed by PM7:Y6, while PM6:Y6 exhibits the slowest recombination. A slower dissociation rate constant (k_d) is estimated for the ASM ZR1:Y6 blend with a slight bias-dependency in charge generation, whereas PM7:Y6 demonstrates bias-independent charge generation despite having similar energetics. Furthermore, same temperature dependency of k_d for all three blends hints at a similar activation energy for CT dissociation. Our morphological investigation shows suppressed π–π stacking of the Y6 aggregates as well as more intermixed domains in the ZR1:Y6 blend. Therefore, we assign the lower k_d of

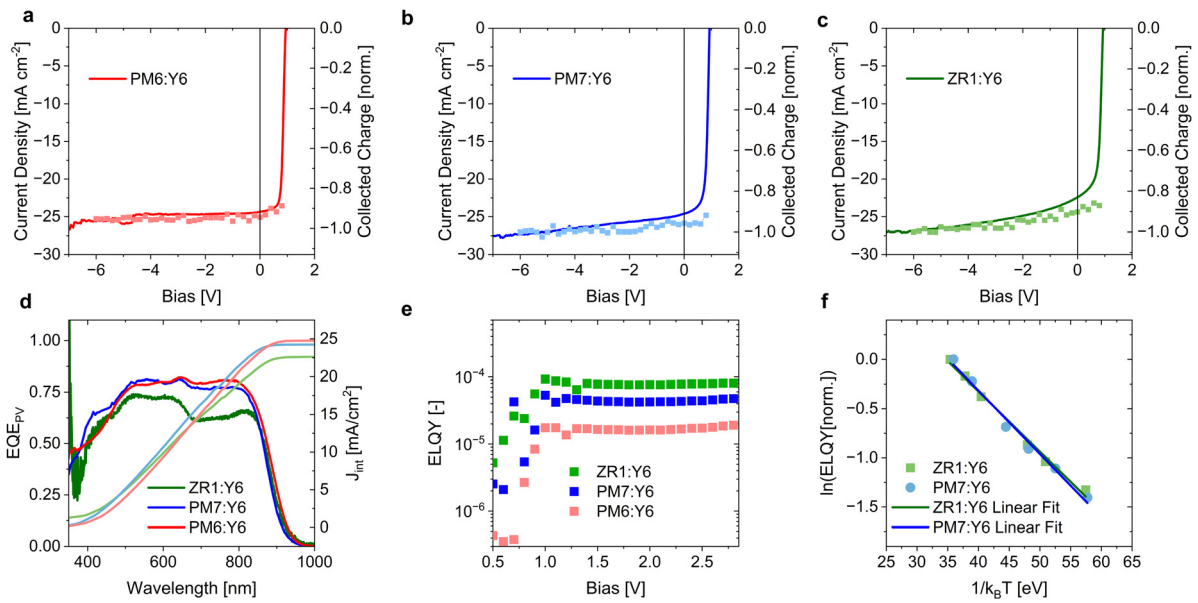

Fig. 1 The curves of the devices with 0.011 cm^2 area (on the left axis) measured under simulated AM1.5G light shown together with the collected charge measured with time-delayed collection field using excitation energy of 2.07 eV and a low fluence of 0.02 μJ cm^{-2} (on the right axis) for (a) PM6:Y6, (b) PM7:Y6 and (c) ZR1:Y6. (d) The photovoltaic external quantum efficiency (EQE_{PV}) of all blends (on the left axis) and the corresponding integrated currents (J_{int}) (e) Electroluminescence quantum yield of organic solar cells as a function of external bias. (f) Temperature dependent electroluminescence measurements are conducted for all systems, the injection current that corresponds to J_{SC} of each system at 1 sun is kept the same for all temperature points. The ΔE_{S_1-CT} values are calculated from the linear fits to the logarithm of the normalized electroluminescence quantum yield with the Arrhenius equation $\left(k_{ref}(T) = k_{ref,0}\exp\left(-\frac{\Delta E_{S_1-CS}}{k_B T}\right)\right)$.

the ASM system to the suppressed mobility and subsequently to its unfavorable molecular orientation and low π–π stacking. Our study exhibits a correlation between the charge carrier mobility, charge recombination and efficient charge generation and addresses the morphological roots of challenges in the ZR1:Y6 system.

Results and discussion

The current–voltage (*J–V*) curves of the ZR1:Y6, PM7:Y6, and PM6:Y6 devices in ITO/PEDOT: PSS/AL/PDINN/Ag structure, are shown in Fig. 1a–c. PM7:Y6 and ZR1:Y6 devices have considerably higher V_{OC} than PM6:Y6. The chemical structure of PM7 differs from PM6 only in terms of the halogen type; PM7 is chlorinated whereas PM6 is fluorinated (chemical structures are shown in Fig. S1, ESI†). Both PM7 and ZR1 donors are reported to have deeper highest occupied molecular orbital (HOMO) energy than PM6 as measured with photoelectron spectroscopy in air (PESA).[29] This is consistent with the increased V_{OC}. However, it should be noted that the lowest unoccupied molecular orbital (LUMO) and HOMO level measurements are prone to numerous limitations and the reported values can have rather large deviation from the actual levels in the bulk.[30] Average short-circuit current densities (J_{SC}) of the PM7:Y6 and PM6:Y6 devices are almost the same (25.6 ± 0.2 and 24.9 ± 0.5 mA cm^{-2}, respectively) and approximately 2 mA cm^{-2} greater than of that ZR1:Y6 (22.6 ± 1.0 mA cm^{-2}). PM6:Y6 has the highest FF of 74.6% followed by PM7:Y6 71.8% and ZR1:Y6 of 68.6%. At the end power conversion efficiency of ZR1:Y6 (14.2%) slightly lacks behind the polymer:Y6 blends. The average device parameters are shown in Table 1 and distributions in Fig. S2 (ESI†).

The bias-dependence of charge generation is measured with time-delayed collection field (TDCF) plotted in Fig. 1a–c (right axis), shown together with the *J–V* (left axis) curves extending to a large negative bias range. A large reverse bias of −6 V is selected to ensure saturation of the current. The *J–V* curve of PM6:Y6 aligns with the TDCF collected charge as a function of bias, and shows no bias-dependency (Fig. 1a). For PM7:Y6 both TDCF and *J–V* data show the same bias-dependency in the negative biases, (Fig. 1b) although in the positive range, *J–V* curve displays a higher bias-dependency. ZR1:Y6 exhibits the highest field dependency of charge generation (Fig. 1c and Fig. S3, ESI†) and the lowest FF. Charge generation efficiencies of blends calculated from the ratio of collected charge at J_{SC} to that at −6V, are tabulated as a measure of the bias-dependency. We select J_{SC} to calculate the charge generation efficiency rather than a value close to V_{OC} because recombination of generated charges with dark injected charges decreases the collected charge in forward biases.[31] The results are presented in Table 1.

From the convolution of the EQE_{PV} and blackbody radiation spectrum, we calculate the same radiative V_{OC} limit ($V_{OC_{rad}}$) of 1.09 V for all systems, with the EQE_{PV} onsets aligning with the Y6 absorption. Moving on to the emission properties, we are able to calculate the non-radiative V_{OC} losses ($\Delta V_{OC_{nrad}}$) of the devices from the electroluminescence quantum yield (ELQY) (Fig. 1e) with $q\Delta V_{OC_{nrad}} = -k_B T \ln(\mathrm{ELQY})$, where q is the elementary charge, k_B is the Boltzmann constant and T the temperature in Kelvin. The largest $\Delta V_{OC_{nrad}}$ is calculated for the PM6:Y6 (0.28 V), followed by the PM7:Y6 (0.25 V) and the lowest value of 0.24 V is estimated for the ASM ZR1:Y6 system. $\Delta V_{OC_{nrad}}$ is affected both from energetic disorder and the D/A energy offsets.[32,33] In order to study the D/A energetics, we consider the energy offset between the singlet S_1 and the CT states. For the blends with sufficiently small ΔE_{S_1-CT}, electroluminescence is almost entirely dominated by the decay of the reformed of S_1 exciton *via* transfer of the charges from CT back to S_1.[34] Temperature dependence of the ELQY reveals the energy barrier from the CT to S_1 state, denoted as ΔE_{S_1-CT}.[21,30] The estimated ΔE_{S_1-CT} values for PM7:Y6 and ZR1:Y6 are the same (64 and 61 meV respectively) (Fig. 1f). The literature value for PM6:Y6 (114 meV)[21] is larger than both PM7:Y6 and ZR1:Y6, a finding consistent with the lower value of V_{OC} observed in PM6:Y6. The larger $\Delta V_{OC_{nrad}}$ in PM6:Y6 may originate from a correspondingly higher barrier of ΔE_{S_1-CT} resulting in a lower exciton reformation efficiency of 0.06% compared to PM7:Y6 and ZR1:Y6 (0.2% and 0.37%, respectively) at room temperature. (Table S1, ESI†) Reformation efficiency of the blend can be estimated by relating the ELQY of the blend to the photoluminescence quantum efficiency (PLQY) of the neat acceptor (photoluminescence spectra of the films are shown in Fig. S5, ESI†).[21]

$\Delta V_{OC_{nrad}}$ has been suggested to exhibit a correlation with the CT energetic disorder which can be related to LUMO disorder (σ_{LUMO}) and HOMO disorder (σ_{HOMO}) $\left(\sigma_{CT} = \sqrt{{\sigma_{LUMO}}^2 + {\sigma_{HOMO}}^2}\right)$.[8] Thus we estimate the static energetic disorder (σ_S) of the HOMO/LUMO levels and the carrier mobility from the transport properties. Charge carrier mobilities of electrons (μ_e) and holes (μ_h) are determined *via* space charge limited current (SCLC) measurements conducted on electron-only and hole-only devices of PM7:Y6 and ZR1:Y6. The PM6:Y6 mobility is taken from our previous study with the same device structure.[35] Ideally, a quadratic relationship is formed between the current and voltage in the space charge limited region. However, slightly higher slopes than 2 are observed due to the field dependent mobility in presence of traps.

Table 1 The average device parameters of PM6:Y6, PM7:Y6 and ZR1:Y6 (of at least 5 devices with 0.06 cm^2 area) are listed with the J_{int} calculated from the EQE_{PV} spectra and charge generation efficiencies calculated by dividing the collected charge at 0 V to the collected charge at −6 V

	V_{OC} [V]	J_{SC} [mA cm^{-2}]	J_{int} [mA cm^{-2}]	FF [%]	PCE [%]	Charge generation efficiency (%)
ZR1:Y6	0.883 ± 0.003	22.6 ± 1.0	21.5	68.6 ± 0.7	14.2 ± 0.4	90
PM7:Y6	0.869 ± 0.002	25.6 ± 0.2	24.4	71.8 ± 0.5	16.3 ± 0.2	95
PM6:Y6	0.838 ± 0.006	24.9 ± 0.5	24.7	74.6 ± 1.6	15.8 ± 0.3	99

Murgatroyd–Gill equation (eqn (1)) is used in order to account for the field effects and estimate the mobilities in zero-field. We use Gaussian disorder model (GDM) (eqn (2)) to calculate σ_S from the temperature dependence of μ_e and μ_h. (SCLC curves and temperature dependent mobility of ZR1:Y6 and PM7:Y6 are shown in Fig. S6, ESI†)

$$V = \frac{9}{8}\mu_0\varepsilon_0\varepsilon_r\frac{V^2}{L^3}\exp\left(0.891\Lambda\sqrt{\frac{V}{L}}\right) \quad (1)$$

Here, Λ is the field enhancement factor, ε_r is the relative permittivity, ε_0 is the vacuum permittivity, L is the active layer thickness, and μ_0 is zero-field mobility.

$$\mu_0(T) = \mu^* \exp\left(-C\left(\frac{\sigma_S}{k_B T}\right)^2\right) \quad (2)$$

Here μ^* is the zero-field mobility at infinite temperature and C is the empirical parameter. For organic semiconductors C can be taken as 0.44 according to previous studies.[36]

The HOMO energetic disorder (σ_{HOMO}) are in the order of PM6:Y6 (78 meV) > PM7:Y6 (70 meV) > ZR1:Y6 (59 meV) and all blends exhibit similar LUMO energetic disorder. ZR1:Y6 blend exhibited surprisingly low electron mobility (μ_e) compared to the two polymer:Y6 blends despite showing similar LUMO disorder (σ_{LUMO}). In a similar vein, the hole mobility (μ_h) of ZR1:Y6, albeit higher than μ_e, is still lower than the polymer:Y6 blends. This is in contrast with the expectation of enhanced charge transport with suppressed energetic disorder. The SCLC μ and σ_s are given in Table 2.

Tenet holds that free charge recombination processes that determine the device V_{OC} take place from the relaxed density of state (DOS).[37,38] For Gaussian DOS, the Fermi energies of these charges can be estimated with Gauss-Fermi integral. In the absence of surface recombination, V_{OC} of a solar cell is equal to the quasi-Fermi level splitting (QFSL) of the electrons and holes ($qV_{OC} = E_{F,e} - E_{F,h}$). Photovoltaic band-gap (E_g) equals the difference between the LUMO energy of the acceptor and the HOMO energy of the donor. There is an energy difference between qV_{OC} and E_g, extent of which depends on σ_S and charge carrier density (n). At high enough temperatures, Fermi level of relaxed holes ($E_{F,h}$) and electrons ($E_{F,e}$) can be determined by the Boltzmann distribution. Hence, temperature dependent V_{OC} is analytically described as:[38,39]

$$qV_{OC} = E_g - \frac{\sigma_{LUMO}{}^2 + \sigma_{HOMO}{}^2}{2k_B T} - 2k_B T \ln\frac{n}{N_0} \quad (3)$$

Here N_0 is the effective DOS, which is approximated from the number density of the acceptor in the blend[34] eqn (3) only holds for low carrier densities. As the temperature goes down, the quasi-Fermi levels cross the equilibrium energy, at which point the transition from the non-degenerate to degenerate region occurs. The analytical approximation for the degenerate range is provided by Paasch and Scheinert[40] (Supplementary note 1 and Fig. S7, ESI†). Temperature dependent carrier densities are obtained from photo-induced absorption (PIA) spectroscopy (Fig. 2a and b). Here, we assign the peaks around 640 nm and 850 nm to ground state bleaching of donors and Y6, respectively. The peak spanning over 900–1100 nm is assigned to polarons.[41,42] Degenerate (low temperature region) and non-degenerate (high temperature region) approximations, using the energetic disorder values (σ_{LUMO}, σ_{HOMO}) obtained by SCLC measurements and E_g of 1.44–1.46 eV as fitting parameter, (Table 3) regenerates the experimental temperature dependent V_{OC} (Fig. 2d). Since the σ_{LUMO} and σ_{HOMO} measured with SCLC belong to the relaxed DOS, this confirms that the recombination processes that determine V_{OC} happens through the relaxed charges.

To assign the low μ of the low disorder ASM system, we turn to the definition of charge transport. μ is widely calculated from the Miller–Abrahams hopping rate of charges from an initial state i with the energy E_i to the next state j with energy E_j (eqn (4)) in the established transport models for organic semiconductors.

$$w_{ij} = \begin{cases} \nu_0 \exp(2\kappa\alpha r_{ij}) \exp\left(-\dfrac{\Delta E_{ij}}{k_B T}\right), & \text{if} \quad \Delta E_{ij} > 0 \\ \nu_0 \exp(2\kappa\alpha r_{ij}), & \text{if} \quad \Delta E_{ij} \le 0 \end{cases} \quad (4)$$

Here w_{ij} is the hopping rate, ν_0 is the attempt to escape frequency, α is the inverse localization length and taken as $\alpha = 10/a$ for a cubic lattice with lattice constant a, κ is the wavefunction overlap parameter, r_{ij} is the separation distance between the two states. Energetic disorder is related to the activation energy for the hopping (ΔE_{ij}). Vithanage *et al.* used kinetic Monte Carlo simulations for a polymer: fullerene blend that ν_0 in the donor domains change depending on the location of the hopping site on the polymer chain.[43] Further, Upreti *et al.* showed that bulk heterojunction blends with same energetic disorder, an order of magnitude difference in mobility can be resulted due to different ν_0 and $\kappa\alpha$ both in fullerene and non-fullerene systems.[44] For similar σ_S, ZR1:Y6 may be explained by lower ν_0, or $\kappa\alpha$ in this system.

In pursuit of elucidating the underlying factors contributing to the lower mobility, we have conducted morphology analysis using grazing incident wide angle X-ray scattering (GIWAXS). The GIWAXS data in Fig. 3a show that the Y6 neat film has face-on π–π stacking preference, as predicted.[25] On the other hand, the ZR1 neat film has significantly higher order and crystallinity compared to Y6 but has an edge-on π–π stacking preference, consistent with literature reports.[45–47] Blending ZR1 with Y6 extensively suppresses the crystallinity of both ZR1 and Y6 (Fig. 3c and d). Fig. S8 (ESI†) shows that PM6 neat film, like Y6 film, has face-on π–π stacking order. The OoP GIWAXS

Table 2 The zero field SCLC electron and mobility values (μ_e, μ_h) are calculated from Murgatroyd/Gill equation at 300 K and the energetic disorder (σ_{LUMO}, σ_{HOMO}) are estimated with the temperature-dependent measurements between 320 K and 220 K for organic blends are listed

	μ_e [cm^2 V^{-1} s^{-1}]	μ_h [cm^2 V^{-1} s^{-1}]	σ_{LUMO} [meV]	σ_{HOMO} [meV]
ZR1:Y6	2.7×10^{-5}	2.8×10^{-4}	63	59
PM7:Y6	1.3×10^{-3}	3×10^{-4}	60	70
PM6:Y6	5.4×10^{-4}	5.5×10^{-4}	60	78

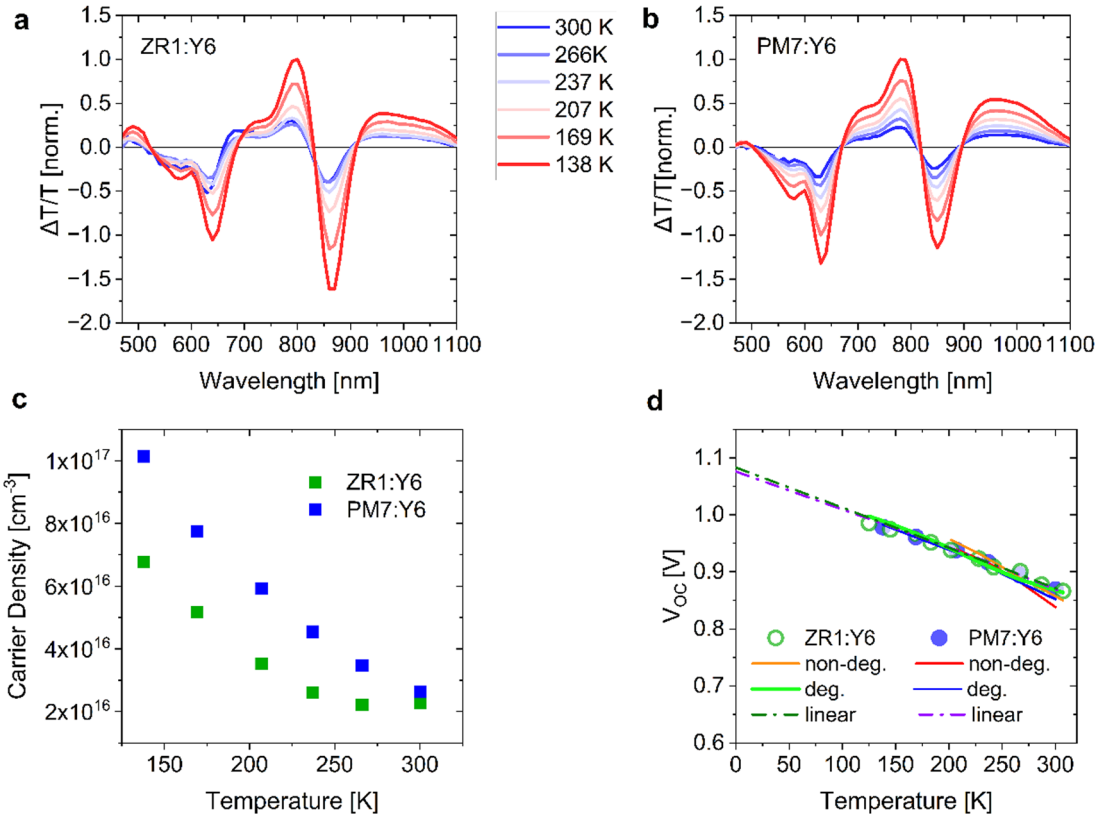

Fig. 2 The temperature dependent photoinduced absorption (PIA) spectra of (a) ZR1:Y6, and (b) PM7:Y6 films on glass with the same active layer thickness with the devices are shown. (c) Calculated charge carrier densities from PIA spectra.[41] (d) Experimental V_{OC} as a function of the temperature (scatters) shown with the Gauss fittings of the degenerate and non-degenerate Gauss-Fermi approximation expression (lines) of PM7:Y6 and ZR1:Y6 devices are shown with the linear extrapolation of the high temperature (300–260 K) experimental data to 0 K (dashed lines) yielding 1.08 V for ZR1:Y6 and 1.07 V for PM7:Y6.

Table 3 The fitting parameter E_g for the estimation of experimental temperature dependent V_{OC} data using σ_{LUMO},σ_{HOMO} values determined *via* SCLC(T) measurements with Gauss-Fermi integral for degenerate and non-degenerate approximations are listed for ZR1:Y6 and PM7:Y6

	Degenerate		Non-degenerate	
	E_g [eV]	σ_{LUMO}, σ_{HOMO} [meV]	E_g [eV]	σ_{LUMO}, σ_{HOMO} [meV]
ZR1:Y6	1.43	59, 63	1.46	59, 63
PM7:Y6	1.44	60, 70	1.46	59, 69
PM6:Y6[a]	1.41	60, 74	1.43	60, 74

[a] Values for PM6:Y6 are taken from the literature,[38] estimated in the same way.

profile of PM6:Y6 (shown in Fig. S8, ESI†), unlike in ZR1:Y6, shows a prominent π–π stacking peak. This PM6:Y6 blend π–π stacking peak is shifted between the original π–π stacking peaks of PM6 and Y6 indicating that both PM6 and Y6 π–π stacking are preserved in the blend and contribute to the blend π–π peak. The main difference here is that the face-on π–π stacking peak remains prominent in the PM6:Y6 blend, but almost disappears in ZR1:Y6 blend (Fig. 3d). For both PM7:Y6 and PM6:Y6 blends our data and literature reports indicate dominant face-on orientation of the π–π stacking with respect of the substrate.[48–50]

We further investigate the active layer mesoscale morphology here since it is known to significantly influence charge carrier mobility and the charge generation in organic blends.[51] The transmission electron microscopy (TEM) and atomic force microscopy (AFM) scans in Fig. 3(e)–(h) show that both PM6:Y6 and ZR1:Y6 films have relatively smooth surfaces and have features on the order of 10s nm. That is consistent with previous reports.[25,45] The ZR1:Y6 film seems slightly rougher than PM6:Y6 with secondary large features on the order of 100s nm, which we interpret as height fluctuations based on the textural resemblance between its AFM and TEM scans (shown in (Fig. 3e and g). Additionally, the surface texture of the ZR1:Y6 film (Fig. 3g) shows no signs of the platelet crystallites that were observed in the neat ZR1 film (Fig. S10, ESI†), in agreement with the GIWAXS results of suppressed crystallinity in ZR1:Y6. We next turn to resonant soft X-ray scattering (RSoXS) to get more insights into domain purity and size of PM6:Y6 and ZR1:Y6 blends. From the RSoXS profiles a scattering feature arises in both blends at the resonant X-ray energy (285.3 eV), Fig. S11 (ESI†), which do not appear at the non-resonant energy (270 eV). This indicates the presence of molecular domains that are uncorrelated with roughness. From these features, characteristic lengths (Lc) which are related to domain size show that ZR1:Y6 has a longer Lc ∼ 60 nm than PM6:Y6 (Lc ∼ 45 nm).

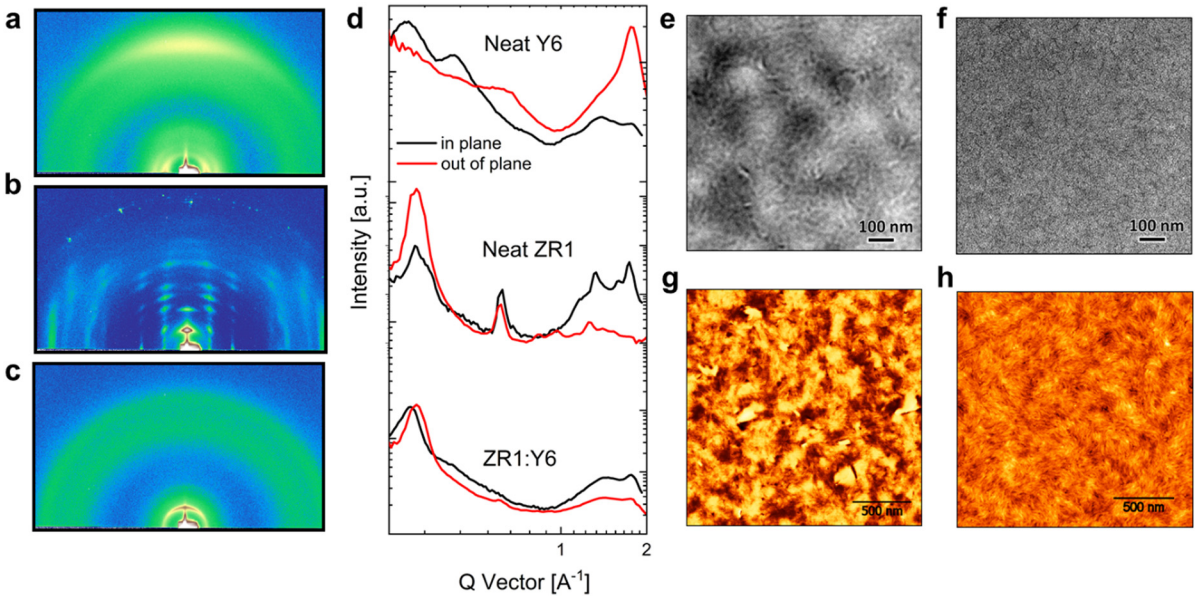

Fig. 3 GIWAXS 2D scans for (a) a neat film of Y6, (b) neat film of ZR1 and (c) ZR1:Y6 blend. (d) 1D GIWAXS profiles extracted from *a*, *b* and *c* scans: in the in-plane direction and in the out-of-plane (OoP) direction. (e) A TEM scan of ZR1:Y6 film (f) a TEM scan of PM6:Y6 film. The scale bars in TEM sans are 100 nm (see Fig. S9, ESI† for zoom series). (g) An AFM scan of ZR1:Y6 film showing an RMS roughness of 1.2 nm. (h) An AFM scan of a PM6:Y6 film showing an RMS roughness of 1 nm (h) the scale bars in the AFM sans are 500 nm.

Additionally, the total scattering intensity, which is proportional to domain purity, is lower for the ZR1:Y6 film than the PM6:Y6 film, which indicates increased mixing of the ZR1:Y6 domains compared with PM6:Y6. By combining the GIWAXS, RSoXS and microscopic results, we conclude that the ZR1:Y6 has mixed and larger domains than PM6:Y6. This is potentially due to an increased thermodynamic miscibility between the two small molecules and a reason for the lower crystallinity. This resulting morphology is the likely origin of ZR1:Y6 having higher recombination coefficient k_2 compared to the polymer:Y6 systems.

The apparent lower charge carrier mobilities of ZR1:Y6 compared to polymer:Y6 blends can be explained with our morphological data showing the lack of parallel stacking of ZR1 and Y6 molecules.[52] In this case, smaller disorder values do not help to facilitate more efficient charge transport due to the unfavorable localization length. In organic semiconductor blends, crystallinity and structural order affect charge generation and recombination. Non-geminate recombination (NGR) coefficients of the blends are measured using PIA and bias assisted charge extraction (BACE) methods. When NGR has a second order dependence on n, recombination rate is given as $R = k_2 n^2$, where k_2 is the bimolecular rate coefficient. Fairly second order kinetics are observed for all systems. Data for recombination rate *versus* carrier density is shown in Fig. S12 (ESI†). Fig. 4a depicts k_2 as a function of carrier density for all the three blends. The k_2 of PM6:Y6 is considerably smaller than the other two systems, in accordance with the recent literature reports on relationship between ΔE_{S_1-CT} and the k_2.[21,30] The k_2 of ZR1:Y6 is slightly higher than PM7:Y6 (Table 4). As a common reference point for the charge recombination in organic semiconductors, Langevin theory outlines the case where whenever two opposite charges meet, they recombine. Therefore, the Langevin rate constant is proportional to charge carrier mobility ($k_L = q(\mu_e + \mu_h)/(\varepsilon_0\varepsilon_r)$). A discrepancy between k_L and k_2 of organic solar cells is commonly observed and the difference between these coefficients is characterized as the Langevin reduction factor (γ). Origin of γ comes from the competition between the CT state decay rate constant (k_f) and charge dissociation rate constant (k_d). If $k_d \gg k_f$ the overall recombination of the free charges is limited by the resplitting of the CT state ($\gamma = k_f/k_d + k_f$). In the resplitting limited regime, k_2 is independent of μ.[53]

We obtain k_d as a function of temperature from temperature-dependent k_2 combined with the temperature-dependent μ values, assuming same k_f of 10^9 s^{-1} for all blends, which is a reasonable value for the organic blends.[54,55] Temperature dependency of k_d are observed to be the same, albeit with a notably lower value for ZR1:Y6 (Fig. 4b). Using the Arrhenius relation, activation energies for charge dissociation were estimated to be similar; 31, 35, and 41 meV for PM6:Y6, PM7:Y6, and ZR1:Y6, respectively (Fig. 4c). This indicates that the lower k_d does not originate from the energy barrier between CT and CS for the ZR1:Y6 blend. In order to find the possible causes of the lower k_d in ZR1:Y6 we turn to the Onsager–Braun theory, which explains charge dissociation in organic blends in terms of local mobility and E_b of the CT state.

$$k_d(F) = \frac{3q(\mu_e + \mu_h)}{4\pi\varepsilon_r\varepsilon_0 R^3} \cdot \exp\left(-\frac{E_b}{k_B T}\right) \cdot \frac{J_1\left(2\sqrt{-2b}\right)}{\sqrt{-2b}} \qquad (5)$$

Here, ε_r is the relative permittivity of the organic material that we took as 3.5 for our calculations, ε_0 is the vacuum permittivity, R is the separation distance of the electron and the hole in the CT exciton, J_1 is the Bessel function in the order of one and

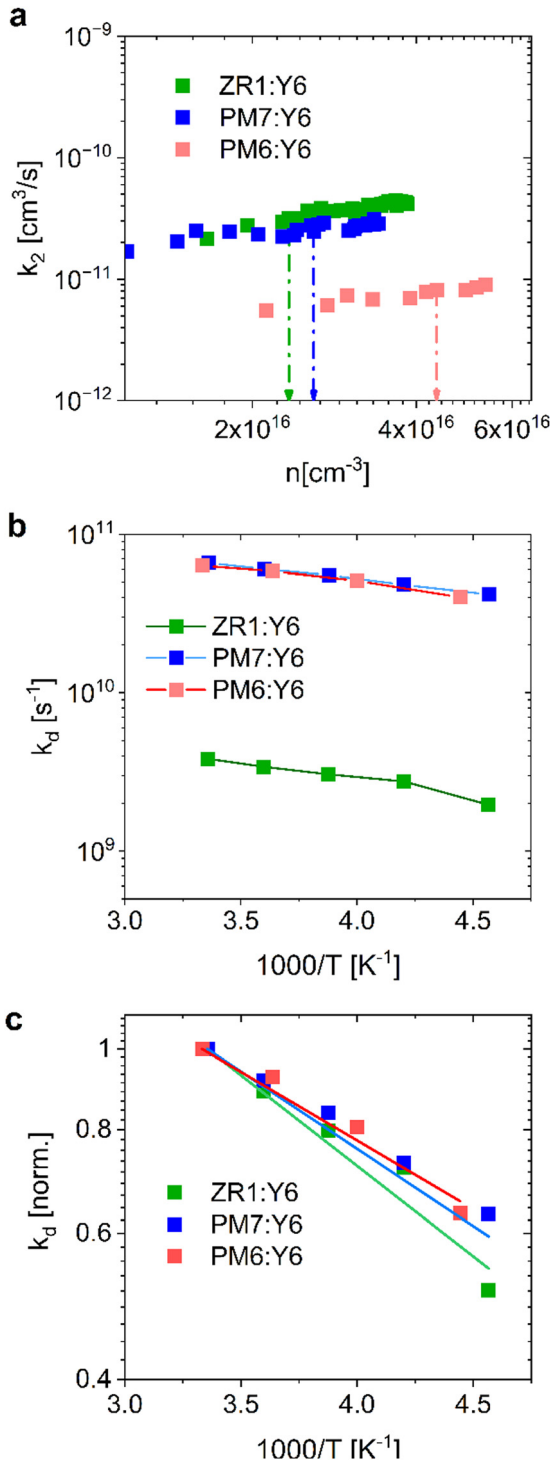

Fig. 4 (a) Bimolecular recombination coefficient *versus* charge carrier density of the ZR1:Y6, PM7:Y6 and PM6:Y6 devices measured with bias-assisted charge extraction with excitation energy of 2.07 eV at V_{OC} conditions. The data point for 1 sun illumination condition for each device is indicated with the dropping lines. (b) The dissociation rate coefficient (k_d) as a function of temperature for each system is shown. (c) Arrhenius fits (lines) to the normalized (k_d) as a function of temperature; entailing similar activation energies for charge generation.

Table 4 Bimolecular rate coefficients of ZR1:Y6, PM7:Y6 and PM6:Y6 devices, measured with bias-assisted charge extraction with an excitation energy of 2.07 eV at 1 sun intensity at room temperature, are tabulated together with the Langevin reduction factor according to the equation $\gamma = k_2/k_L$

	k_2 [cm^3 s^{-1}]	γ
ZR1:Y6	4.3×10^{-11}	0.260
PM7:Y6	1.3×10^{-11}	0.015
PM6:Y6	8×10^{-12}	0.014

$b = q^3F/(8\pi\varepsilon_r\varepsilon_0(k_BT)^2)$ and E_b is the binding energy $\left(E_b = \frac{q^2}{4\pi\varepsilon_r\varepsilon_0 R}\right)$. Nevertheless, our morphological data shows that in the ZR1:Y6 blend, molecules do not have a regular alignment, which is expected to have a detrimental effect on mobility. According to the Onsager–Braun theory, k_d is proportional to the sum of mobility. Accordingly, the lower sum of mobility in ZR1:Y6 impacts the dissociation efficiency. In polymer:Y6 blends both D and A domains take a face-on orientation, which benefits charge generation. In this regard, the main challenge for the ZR1:Y6 blend originates from the necessity to control morphology, which significantly influences charge carrier mobility and the charge generation in organic blends.[51]

Conclusions

Our data show that for the ZR1:Y6 and PM7:Y6 blends, the V_{OC} losses are suppressed compared to PM6:Y6. Deeper reported HOMO levels of PM7 and ZR1 result in smaller ΔE_{S_1-CT}, translating to the suppression of the E_g losses. Concomitantly, the thermal population of the S_1 states by the back transfer of the charges from the CT reduces the $\Delta V_{OC_{nrad}}$ in PM7:Y6 and ZR1:Y6, compared to PM6:Y6. We show that despite the lower disorder in the ZR1:Y6 blend, the mobility remains low. Unfavorable alignment and insufficient π–π stacking with intermixed domains of ZR1:Y6 compared to the polymer:Y6 devices exhibit a difficulty for hopping transport. Polymer donors confer an advantage by facilitating a superior face-on order and maintaining the π–π stacking of the Y6 molecules, thus establishing conducting channels between ordered domains. ZR1:Y6 exhibits the strongest field-dependency of charge generation among the systems in the study. Recent studies show that decreasing the ΔE_{S_1-CT} at the D/A interface comes at a price of the suppressed charge generation due to the lower probability of the CT formation.[21,30,56] With temperature-dependent electroluminescence measurements, we estimated the same ΔE_{S_1-CT} for PM7:Y6 and ZR1:Y6. Confirming the similar energetics, we anticipated a similar behavior in charge generation as a function of the field for the ZR1:Y6 blend. However, contrary to expectations, we observe a higher field-dependency in the ZR1:Y6 system. Temperature dependency of the k_d remains close across both systems, suggesting a similar activation energy for charge generation. Nevertheless, there is a significant difference in the Langevin reduction factor of ZR1:Y6 and polymer:Y6 blends, hinting at a lower k_d in ZR1:Y6. A viable explanation lies in the lower μ in this system. While not insisting on the actual values of the k_f and k_d, our data underscore the

importance of μ for CT dissociation. In these two systems, the determining factor for free charge generation appears to be the morphology rather than the energetic landscape.

As an outlook for future studies, it is worthwhile to consider the role of delocalization in charge generation. Our study has demonstrated that charge separation is more efficient with polymer donors compared to small molecule donors, likely due to greater hole delocalization in polymers. The significance of hole delocalization for charge separation is well-documented in the literature.[57] For example, Nenashev *et al.* reported that delocalization of holes along polymer chains increases the probability of exciton dissociation using a semi-analytic model for polymer blends.[58] Similarly, Y6, a small molecule, also shows strong polaron delocalization, which greatly enhances charge generation.[59] Crystallinity and packing are crucial factors that promote higher charge delocalization in both polymers and small molecules. Therefore, future studies should investigate the effects of delocalization on polymers *versus* small molecules to better understand why polymer donors consistently outperform small molecule donors. A comprehensive study involving a broader selection of small molecule and polymer donors would be necessary to draw general conclusions and would be of great interest to the community.

Data availability

The data supporting this article have been included as part of the ESI.†

Conflicts of interest

There are no conflicts to declare.

Acknowledgements

We acknowledge support by the German Research Foundation through the project Fabulous, project numbers 450968074. BAC, AP, and TM acknowledge funding support from the US National Science Foundation under grant number 2247711. We thank the MJ Murdock Charitable Trust for funding of the Xuess 3.0 X-ray scattering beamline. This research used beamline 7-1-ID (SST-1) of the National Synchrotron Light Source II, a U.S. Department of Energy (DOE) Office of Science User Facility operated for the DOE Office of Science by Brookhaven National Laboratory under Contract No. DE-SC0012704.

References

1 B. Kan, Y. Kan, L. Zuo, X. Shi and K. Gao, *InfoMat*, 2021, **3**, 175–200.
2 M. Shi, T. Wang, Y. Wu, R. Sun, W. Wang, J. Guo, Q. Wu, W. Yang and J. Min, *Adv. Energy Mater.*, 2021, **11**, 1–11.
3 S. Samson, J. Rech, L. Perdigón-Toro, Z. Peng, S. Shoaee, H. Ade, D. Neher, M. Stolterfoht and W. You, *ACS Appl. Polym. Mater.*, 2020, **2**, 5300–5308.
4 Y. Wang, J. Lee, X. Hou, C. Labanti, J. Yan, E. Mazzolini, A. Parhar, J. Nelson, J. S. Kim and Z. Li, *Adv. Energy Mater.*, 2021, **11**, 1–41.
5 P. Kaienburg, A. Jungbluth, I. Habib, S. V. Kesava, M. Nyman and M. K. Riede, *Adv. Mater.*, 2022, **34**, 2107584.
6 P. Kaienburg, H. Bristow, A. Jungbluth, I. Habib, I. McCulloch, D. Beljonne and M. Riede, *ACS Appl. Mater. Interfaces*, 2023, **15**, 31684–31691.
7 S. D. Collins, C. M. Proctor, N. A. Ran and T. Q. Nguyen, *Adv. Energy Mater.*, 2016, **6**, 1–11.
8 S. M. Hosseini, S. Wilken, B. Sun, F. Huang, S. Y. Jeong, H. Y. Woo, V. Coropceanu and S. Shoaee, *Adv. Energy Mater.*, 2023, **13**, 2203576.
9 Q. Liu and K. Vandewal, *Adv. Mater.*, 2023, **35**, 2302452.
10 X. K. Chen, D. Qian, Y. Wang, T. Kirchartz, W. Tress, H. Yao, J. Yuan, M. Hülsbeck, M. Zhang, Y. Zou, Y. Sun, Y. Li, J. Hou, O. Inganäs, V. Coropceanu, J. L. Bredas and F. Gao, *Nat. Energy*, 2021, **6**, 799–806.
11 Y. Sun, L. Nian, Y. Kan, Y. Ren, Z. Chen, L. Zhu, M. Zhang, H. Yin, H. Xu, J. Li, X. Hao, F. Liu, K. Gao and Y. Li, *Joule*, 2022, **6**, 2835–2848.
12 J. Ge, L. Hong, H. Ma, Q. Ye, Y. Chen, L. Xie, W. Song, D. Li, Z. Chen, K. Yu, J. Zhang, Z. Wei, F. Huang and Z. Ge, *Adv. Mater.*, 2022, **34**, 1–9.
13 Y. Wei, Z. Chen, G. Lu, N. Yu, C. Li, J. Gao, X. Gu, X. Hao, G. Lu, Z. Tang, J. Zhang, Z. Wei, X. Zhang and H. Huang, *Adv. Mater.*, 2022, **34**, 2204718.
14 D. Li, N. Deng, Y. Fu, C. Guo, B. Zhou, L. Wang, J. Zhou, D. Liu, W. Li, K. Wang, Y. Sun and T. Wang, *Adv. Mater.*, 2023, **35**, 2208211.
15 L. Zhu, J. Zhang, Y. Guo, C. Yang, Y. Yi and Z. Wei, *Angew. Chem., Int. Ed.*, 2021, **60**, 15348–15353.
16 L. Zhu, Z. Tu, Y. Yi and Z. Wei, *J. Phys. Chem. Lett.*, 2019, **10**, 4888–4894.
17 Y. Zhu, F. Zhao, W. Wang, Y. Li, S. Zhang and Y. Lin, *Adv. Energy Sustainable Res.*, 2022, **3**, 2100184.
18 M. B. Price, P. A. Hume, A. Ilina, I. Wagner, R. R. Tamming, K. E. Thorn, W. Jiao, A. Goldingay, P. J. Conaghan, G. Lakhwani, N. J. L. K. Davis, Y. Wang, P. Xue, H. Lu, K. Chen, X. Zhan and J. M. Hodgkiss, *Nat. Commun.*, 2022, **13**, 1–10.
19 E. Sağlamkaya, A. Musiienko, M. S. Shadabroo, B. Sun, S. Chandrabose, O. Shargaieva, G. M. Lo Gerfo, N. F. Van Hulst and S. Shoaee, *Mater. Horiz.*, 2023, 1825–1834.
20 L. Perdigón-Toro, H. Zhang, A. Markina, J. Yuan, S. M. Hosseini, C. M. Wolff, G. Zuo, M. Stolterfoht, Y. Zou, F. Gao, D. Andrienko, S. Shoaee and D. Neher, *Adv. Mater.*, 2020, **32**, 1906763.
21 B. Sun, N. Tokmoldin, O. Alqahtani, A. Patterson, C. S. P. De Castro, D. B. Riley, M. Pranav, A. Armin, F. Laquai, B. A. Collins, D. Neher and S. Shoaee, *Adv. Energy Mater.*, 2023, **13**, 2300980.
22 W. Li, S. Zeiske, O. J. Sandberg, D. B. Riley, P. Meredith and A. Armin, *Energy Environ. Sci.*, 2021, **14**, 6484–6493.
23 Y. Fu, T. H. Lee, Y. C. Chin, R. A. Pacalaj, C. Labanti, S. Y. Park, Y. Dong, H. W. Cho, J. Y. Kim, D. Minami, J. R. Durrant and J. S. Kim, *Nat. Commun.*, 2023, **14**, 1870.

24 L. Zhu, M. Zhang, G. Zhou, T. Hao, J. Xu, J. Wang, C. Qiu, N. Prine, J. Ali, W. Feng, X. Gu, Z. Ma, Z. Tang, H. Zhu, L. Ying, Y. Zhang and F. Liu, *Adv. Energy Mater.*, 2020, **10**, 1–9.
25 O. Alqahtani, A. Alotaibi, M. Burnes and B. A. Collins, *ACS Energy Lett.*, 2023, **8**, 4643–4649.
26 S. Riera-Galindo, M. Sanz-Lleó, E. Gutiérrez-Fernández, N. Ramos, M. Mas-Torrent, J. Martín, L. López-Mir and M. Campoy-Quiles, *Small*, 2024, **2311735**, 1–12.
27 S. M. Hosseini, N. Tokmoldin, Y. W. Lee, Y. Zou, H. Y. Woo, D. Neher and S. Shoaee, *Sol. RRL*, 2020, **4**, 2000498.
28 O. Alqahtani, J. Lv, T. Xu, V. Murcia, T. Ferron, T. McAfee, D. Grabner, T. Duan and B. A. Collins, *Small*, 2022, **18**, 1–13.
29 J. Bertrandie, J. Han, C. S. P. De Castro, E. Yengel, J. Gorenflot, T. Anthopoulos, F. Laquai, A. Sharma and D. Baran, *Adv. Mater.*, 2022, **34**, 2202575.
30 N. Tokmoldin, B. Sun, F. Moruzzi, A. Patterson, O. Alqahtani, R. Wang, B. A. Collins, I. McCulloch, L. Lüer, C. J. Brabec, D. Neher and S. Shoaee, *ACS Energy Lett.*, 2023, **8**, 2552–2560.
31 B. Gerber, N. Tokmoldin, O. J. Sandberg, E. Sağlamkaya, B. Sun, S. Shoaee and D. Neher, *Sol. RRL*, 2024, **8**, 2400083.
32 D. Qian, S. M. Pratik, Q. Liu, Y. Dong, R. Zhang, J. Yu, N. Gasparini, J. Wu, T. Zhang, V. Coropceanu, X. Guo, M. Zhang, J. L. Bredas, F. Gao and J. R. Durrant, *Adv. Energy Mater.*, 2023, **13**, 1–9.
33 T. Fritsch, J. Kurpiers, S. Roland, N. Tokmoldin, S. Shoaee, T. Ferron, B. A. Collins, S. Janietz, K. Vandewal and D. Neher, *Adv. Energy Mater.*, 2022, **12**, 2200641.
34 L. Perdigón-Toro, L. Q. Phuong, S. Zeiske, K. Vandewal, A. Armin, S. Shoaee and D. Neher, *ACS Energy Lett.*, 2021, **6**, 557–564.
35 E. Sağlamkaya, S. M. Hosseini, N. Tokmoldin, A. Musiienko, T. Krüger, J. Behrends, M. Raoufi, D. Neher and S. Shoaee, *Sol. RRL*, 2023, **10**, 1–8.
36 H. Bässler, *Phys. Status Solidi*, 1993, **175**, 15–56.
37 K. Vandewal, S. Albrecht, E. T. Hoke, K. R. Graham, J. Widmer, J. D. Douglas, M. Schubert, W. R. Mateker, J. T. Bloking, G. F. Burkhard, A. Sellinger, J. M. J. Fréchet, A. Amassian, M. K. Riede, M. D. McGehee, D. Neher and A. Salleo, *Nat. Mater.*, 2014, **13**, 63–68.
38 L. Perdigón-Toro, L. Q. Phuong, F. Eller, G. Freychet, E. Saglamkaya, J. I. Khan, Q. Wei, S. Zeiske, D. Kroh, S. Wedler, A. Köhler, A. Armin, F. Laquai, E. M. Herzig, Y. Zou, S. Shoaee and D. Neher, *Adv. Energy Mater.*, 2022, **12**, 2103422.
39 J. C. Blakesley and D. Neher, *Phys. Rev. B: Condens. Matter Mater. Phys*, 2011, **84**, 075210.
40 G. Paasch and S. Scheinert, *J. Appl. Phys.*, 2010, **107**, 104501.
41 L. Q. Phuong, S. M. Hosseini, O. J. Sandberg, Y. Zou, H. Y. Woo, D. Neher and S. Shoaee, *Sol. RRL*, 2021, **5**, 1–6.
42 B. Sun, O. J. Sandberg, D. Neher, A. Armin and S. Shoaee, *Phys. Rev. Appl*, 2022, **17**, 1–12.
43 D. A. Vithanage, A. Devižis, V. Abramavičius, Y. Infahsaeng, D. Abramavičius, R. C. I. MacKenzie, P. E. Keivanidis, A. Yartsev, D. Hertel, J. Nelson, V. Sundström and V. Gulbinas, *Nat. Commun.*, 2013, **4**, 2334.
44 T. Upreti, Y. Wang, H. Zhang, D. Scheunemann, F. Gao and M. Kemerink, *Phys. Rev. Appl.*, 2019, **12**, 1.
45 R. Zhou, Z. Jiang, C. Yang, J. Yu, J. Feng, M. A. Adil, D. Deng, W. Zou, J. Zhang, K. Lu, W. Ma, F. Gao and Z. Wei, *Nat. Commun.*, 2019, **10**, 1–9.
46 W. A. Memon, R. Zhou, Y. Zhang, Y. Wang, L. Liu, C. Yang, J. Zhang, A. Liaqat, L. Xie and Z. Wei, *Adv. Funct. Mater.*, 2022, **32**, 1–10.
47 C. Zhang, Y. Zhang, Z. Wang, Y. Su, Z. Wei, J. Hou, S. He, K. Wu, C. He, J. Zhang and C. Wang, *Sci. China: Chem.*, 2021, **64**, 1569–1576.
48 M. Zhang, L. Zhu, G. Zhou, T. Hao, C. Qiu, Z. Zhao, Q. Hu, B. W. Larson, H. Zhu, Z. Ma, Z. Tang, W. Feng, Y. Zhang, T. P. Russell and F. Liu, *Nat. Commun.*, 2021, **12**, 1–10.
49 R. Ma, T. Liu, Z. Luo, Q. Guo, Y. Xiao, Y. Chen, X. Li, S. Luo, X. Lu, M. Zhang, Y. Li and H. Yan, *Sci. China: Chem.*, 2020, **63**, 325–330.
50 H. Liang, Y. Wang, X. Guo, D. Yang, X. Xia, J. Wang, L. Zhang, Y. Shi, X. Lu and M. Zhang, *J. Mater. Chem. A*, 2022, **10**, 10926–10934.
51 C. M. Proctor, S. Albrecht, M. Kuik, D. Neher and T. Q. Nguyen, *Adv. Energy Mater.*, 2014, **4**, 1400230.
52 R. Yu, S. Li, H. Yuan, Z. Yang, S. Jin and Z. Tan, *J. Phys. Chem. Lett.*, 2024, **15**, 2781–2803.
53 G. Zuo, S. Shoaee, M. Kemerink and D. Neher, *Phys. Rev. Appl.*, 2021, **16**, 1.
54 A. Armin, J. R. Durrant and S. Shoaee, *J. Phys. Chem. C*, 2017, **121**, 13969–13976.
55 S. Ichiro Natsuda, T. Saito, R. Shirouchi, K. Imakita and Y. Tamai, *Polym. J.*, 2022, **54**, 1345–1353.
56 M. Pranav, T. Hultzsch, A. Musiienko, B. Sun, A. Shukla, F. Jaiser, S. Shoaee and D. Neher, *APL Mater.*, 2023, **11**, 061111.
57 Y. Tamai, *Polym. J.*, 2020, **52**, 691–700.
58 A. V. Nenashev, M. Wiemer, F. Jansson and S. D. Baranovskii, *J. Non. Cryst. Solids*, 2012, **358**, 2508–2511.
59 G. Zhang, X.-K. Chen, J. Xiao, P. C. Y. Chow, M. Ren, G. Kupgan, X. Jiao, C. C. S. Chan, X. Du, R. Xia, Z. Chen, J. Yuan, Y. Zhang, S. Zhang, Y. Liu, Y. Zou, H. Yan, K. S. Wong, V. Coropceanu, N. Li, C. J. Brabec, J.-L. Bredas, H.-L. Yip and Y. Cao, *Nat. Commun.*, 2020, **11**, 3943.

